Electronic Supplementary Information (ESI) for Energy & Environmental Science

Atomic-Level Engineering $Fe_1N_2O_2$ Interfacial Structure Derived from Oxygen-Abundant Metal–Organic Frameworks to Promote Electrochemical CO_2 Reduction

Di Zhao,‡[a] Ke Yu,‡[b] Pengyu Song,‡[a] Wuyi Feng,[a] Botao Hu,[c] Weng-Chon (Max) Cheong,[d] Zewen Zhuang,[b] Shoujie Liu,*[b] Kaian Sun,[b] Jiatao Zhang,*[a] Chen Chen*[b]*

[a]*Key Laboratory of Cluster Science, Ministry of Education of China, Beijing Key Laboratory of Photoelectronic/Electrophotonic Conversion Materials, School of Chemistry and Chemical*
[b]*Engineering, Beijing Institute of Technology, Beijing 100081, China*
Department of Chemistry, Tsinghua University, Beijing 100084 (China)
[c]*Qian Xuesen Laboratory of Space Technology China Academy of Space echnology Beijing 100094, P. R. China*
[d]*Department of Physics and Chemistry, Faculty of Science and Technology, University of Macau, Macao SAR, P. R. China*
‡ These authors contributed equally to this work.

Experimental Section

Synthesis of one-dimensional Fe/Zn-MOF-74 and Zn-MOF-74 nanorods.

Fe/Zn-MOF-74 nanorods were prepared according to a modified solvothermal method in other literature.[1] Anhydrous zinc acetate ($Zn(O_2CCH_3)_2$; 0.35 g, 1.91mmol) and anhydrous iron acetate (3 mg) were dissolved in 20 ml DMF solution with stirring in flask A. 2,5-dihydroxyterephthalic acid (0.25 g, 1.26 mmol) was dissolved in 20 ml DMF solution under ultrasound for 5 min to form a clear solution in flask B. Salicylic acid (0.055 g, 0.40 mmol) was dissolved in 5 ml DMF solution in flask C. Then solution in flask B was added dropwise into flask A with vigorous stirring. After stirring for 10 min, the solution in flask C was added dropwise into flask A with vigorous stirring. The resulting yellow precipitate was kept stirring for 2 h. Then the resulting yellow precipitate was kept undisturbed at room temperature for 30 min and finally separated by centrifugation. The obtained product was subsequently washed with DMF (3 × 30 ml) and methanol (3 × 30 ml) to remove excess reactants and modulator. The yellow material obtained after washing was suspended in 30 ml anhydrous methanol and heated at 120 °C for 36 h in a 50 ml Teflon-lined autoclave. After cooling to room temperature, the mother liquor was decanted and the resultant yellow powder was washed with methanol (3 × 30 ml) and activated under dynamic vacuum at 60 °C for 24 h to yield the solvent-free MOF-74 nanorod. Zn-MOF-74 nanorods were prepared by the same method with Fe/Zn-MOF-74 without adding iron source in flask A.

Synthesis of $Fe_1N_2O_2$/NC and NC.

150 mg dried Fe/Zn-MOF-74 and a certain amount of melamine were dissolved in a solution containing 3 mL of methanol. After being stirred for 60 min, the obtained suspension was treated under vacuum at 60 °C for 12 h. Then the as-prepared compound was placed in a ceramic boat and transferred into a temperature-programmed furnace. The pyrolysis treatment was performed at 1000 °C for 3 h with a heating rate of 3°C/min under Ar atmosphere. The obtained samples were donated as $Fe_1N_2O_2$/NC. For comparison, the sample of pure nitrogen doped carbon, NC, was also synthesized by a similar method with Zn-MOF-74 as precursor.

Synthesis of Fe_n/C confined in one-dimensional nanorods.

The powder of Fe/Zn-MOF-74 was placed in a tube furnace and then heated at 1000 °C for 3 h with a heating rate of 3°C/min under Ar atmosphere.

Characterizations.

X-ray diffraction (XRD) patterns were collected on a Model D8 Avance X-ray diffractometer (Bruker, Germany) with Cu Kα radiation. TEM and HRTEM images were recorded using a Hitachi HT7700 instrument working at 100 kV and an FEI Tecnai G2 F20 S-Twin working at 200 kV. HAADF images were taken on a JEM-ARM200F atomic-resolution analytical microscope operated at 300 kV. ICP-OES was measured by a Thermo Fisher IRIS Intrepid α system. X-ray photoelectron spectroscopy (XPS) was performed on a ULVAC PHI Quantera microscope. Laser confocal Raman spectrometer was operated on a HR-800. N_2 adsorption-desorption

experiments were carried out at 77 K on a Quantachrome SI-MP Instrument. The surface area of the samples was estimated by method of Brunauer-Emmett-Teller (BET). X-ray absorption spectroscopy (XAS) measurement and data analysis: X-ray absorption near-edge spectra (XANES) at the Fe K-edge obtained at 1W1B station in BSRF (Beijing Synchrotron Radiation Facility, P. R. China) and labxafs, Rapidxafs 1M. The C-edge and N-edge were measured at beamline BL12B of National Synchrotron Radiation Laboratory (NSRL) in Hefei of China and the samples were deposited onto double-sided carbon tap.

Electroreduction of CO_2 in a H-type cell.

The electrolyte was prepared by bubbling CO_2 into the sodium carbonate aqueous solution (0.1 M) overnight. The H-type cell was used as the electrolyzer for CO_2 electrochemical reduction. All the water used in the CO_2 RR was ultrapure water (18.2 MΩ cm). A Nafion 117 membrane was inserted between the cathodic and anodic chambers. A mass flow controller was used to set the CO_2 flow rate at 20 sccm. Sigracet 39 BC carbon paper, Pt wire and Ag/AgCl were used as working electrode, counter electrode and reference electrode respectively. The linear sweep voltammetry curves were recorded with a CHI 760 electrochemical workstation with a scan rate of 10 mV s^{-1}. All the potential were reported with respect to the reversible hydrogen electrode (RHE). ECSA referred the CV results under the potential windows of -0.1 - 0.5 V (vs RHE). C_{dl} is determined by linear fittings of the differences of current densities between anodic scans and cathodic scans with the scan rates. The chronoamperometry tests were conducted at each potential for 40min. The gas products of electrolysis were detected on the Shimazu 2010 plus gas chromatography equipped with BID detector and ShinCarbon ST 100/120 packed column. High purity helium (99.9999%) was used as the carrier gas for the chromatography. The Faraday efficiency of gas products was calculated by the equation:

$$FE = \frac{2 \times 96485\left(\frac{c}{mol}\right) \times V\left(\frac{mL}{min}\right) \times 10^{-6}\left(\frac{m3}{mL}\right) \times v\,(vol\,\%) \times 1.013 \times 10^{5}\left(\frac{N}{m^2}\right)}{8.314\left(N \cdot \frac{m}{mol \cdot K}\right) \times 298.15\,K \times I_{total}\left(\frac{C}{s}\right) \times 60\left(\frac{s}{min}\right)}$$

ν (vol %) = volume concentration of CO in the exhaust gas from the cell (GC data). V (mL/min) = Gas flow rate measured by a flow meter at the exit of the cell at room temperature and under ambient pressure. I_{total} (C/s) = steady-state cell current.

Both CO_2 reduction and HER make contribution for the current in aqueous electrolyte. No liquid products are detected after electrolysis. CO is the main product of CO_2 electrolysis for $Fe_1N_2O_2$/NC.

Electroreduction of CO_2 in a gas-diffusion electrodes (GDE) -based flow electrolyzer.

Electrochemical Measurements at high current densities was performed in a flow cell (Gaossunion, 101017-1.2) (Fig. 5a) using constant potential electrolysis method. Carbon paper coated with catalyst, Ag/AgCl (saturated KCl) electrode, and a Pt plate (1.0 cm×3.0 cm,) were used as cathode (for CO_2 reduction), reference electrode and

anode (for O_2 evolution), respectively. The catalyst ink was prepared by adding 48 mg $Fe_1N_2O_2$/NC into a mixed solution of 4 mL isopropanol/water (50%(v/v)), 50 μL PTFE dispersion (Daikin D-210C, 55%) and 80 μL Nafion solution (DuPont D520, 5 wt%), and then was ultrasonically treated for 1 hour to form a homogeneous ink. The gas diffusion electrode (GDE) was prepared by spraying the above ink with an airbrush on carbon paper (SIGRACET 29BC). The catalyst-loading density was about 2.0 mg/cm^2. Cathode and anode are respectively connected with copper tape (current collector). Catholyte and anolyte chambers had an inlet and an outlet for electrolyte, CO_2 gas diffusion chamber had an inlet and an outlet for CO_2 gas, and Ag/AgCl electrode was fixed in catholyte chamber. Catholyte and anolyte chambers were separated by an anionexchange membrane (Fumasep, FAB-PK-130), and a silicone gasket was placed between each GDE, anionic exchange membrane and electrolyte chamber for sealing when assembling the flow cell. Catholyte (1 M KOH) was circulated in cathode chamber by using a conventional peristaltic pump, while anolyte (1 M KOH) was circulated through anode chamber by using a specially-made gas-liquid mixed flow pump. CO_2 was delivered to the back chamber of catholyte chamber at a constant flow 40 sccm by mean of a digital mass flow controller.

Computational details

A series of spin polarized density functional theory (DFT) calculations were all done with the Vienna Ab initio Simulation Package (VASP).[2] The electron-ion interaction was described using the projector augmented wave (PAW),[3] and the kinetic energy cutoff for plane wave expansions was set to 520 eV. The electron exchange and correlation energies were treated within a generalized gradient approximation (GGA) in the Perdew-Burke-Ernzerhof (PBE) exchange-correlation.[4] A DFT-D3 scheme of dispersion correction was used to describe the van der Waals (vdW) interactions in molecule adsorption.[5] The Brillouin zone was sampled using the Monkhorst-Pack 3×3×1 sampling[6] and the convergence criteria were 1×10^{-6} eV and 1×10^{-8} eV energy differences for solving for the electronic wave function in structure optimization and vibrational frequency calculations, respectively, and force convergence criterion of -0.02 eV Å^{-1}. To avoid the interactions between two adjacent periodic images, the vacuum thickness was set to be 20 Å. The electron smearing width of $\sigma = 0.05$ eV was employed according to the Methfessel-Paxton technique. The free energy correction was obtained similarly by including the zero-point energy (ZPE) and entropic contributions from vibrational degrees of freedom calculated with the substrate fixed, and the value gained by using Vaspkit.1.2.5.[7] A 6x6 supercell consisting of 72 carbon atoms from a graphene conventional cell of the lattice parameters of a=2.46Å, b=2.46Å and α=β=90°, γ=120° was used firstly, then deleted two connected carbon atoms for formed a defect, and C atoms were substituted by two N atoms and two O atoms in the innermost layer at the defect. Then a Fe atom was embedded in the defect to form the $Fe_1N_2O_2$. Using similar approach to obtain the models of Fe_1N_4 and Fe_1N_3O, Fe_1NO_3 and Fe_1O_4, respectively.

The binding energy was calculated by subtracting the energies of the isolated adsorbate and the catalyst from the total energy of the adsorbed system:

E_b = E (slab + adsorbate) - E (slab) - E (adsorbate)

The pathway by which the CO_2RR occurs under base condition are generally reported to proceed according to the following step:

1 $CO_2 + H^+ + e^- + * \rightarrow *COOH$

2 $*COOH + H^+ + e^- \rightarrow *CO + H_2O$

3 $*CO \rightarrow * + CO$

Where the * refers to the catalytic, and the *one refers to the species that adsorbed on the activity sites.

Neglect PV contribution to translation for adsorbed molecules, the free energy of every step was calculated according to the equation of $G = E + H_{cor} - TS = E + G_{cor}$, where E is the energy of every specie obtained from DFT calculations, and S are entropy, while T is 298.15 K. The H_{cor} and G_{cor} are the thermal correction to enthalpy and the thermal correction to Gibbs free energy, respectively. The G_{cor} of *COOH and *CO were taken from the frequency DFT calculation and got value by using Vaspkit.1.2.5.

The Gibbs free energy of the proton-electron pairs ($H^+ + e^-$) related in the PECT progress,[8] whereas the fact that the proton-electron pairs is in equilibrium with gaseous H_2 at 0 V versus standard hydrogen electrode (U = 0, pH = 0, and pressure = 1 bar, and temperature = 298.15K):

$\mu(H^+ + e^-) = 1/2\ \mu(H_2\ (g))$

According to Vaspkit.1.2.5, the internal energy of gas molecular gained from the formula: $U(T) = ZPE + \Delta U(0\text{-}T)$, the enthalpy of gas molecular gained from the formula: $H(T) = U(T) + PV = ZPE + \Delta U(0\text{-}T) + PV$, and the Gibbs free energy of gas molecular gained from the formula: $G(T) = H(T) - TS = ZPE + \Delta U(0\text{-}T) + PV - TS = E\_DFT + G_{cor}'$.

Where E_DFT is the energy of the free gas molecule obtained from DFT calculations, G_{cor}' is the thermal correction to Gibbs free energy of the free gas molecule obtained from the frequency DFT calculation and got value by using Vaspkit.1.2.5, with the temperature of 298.15K, the pressure of CO_2 and CO, H_2O and H_2 were 1 atm and 1 atm, 0.035 atm and 1 atm, respectively, and all species input 1 as the value of spin multiplicity.

The d-band center[9] of the 3d orbitals of Fe obtained from their PDOS by using equation:

$$\varepsilon_d = \frac{\int_{-\infty}^{+\infty} \varepsilon f(\varepsilon) d\varepsilon}{\int_{-\infty}^{+\infty} f(\varepsilon) d\varepsilon}$$

where, the f(ε) is the PDOS of an energy level of ε.

The charge density difference was evaluated using the formula $\Delta\rho = \rho(\text{Co/substrate}) - \rho(\text{Co}) - \rho(\text{substrate})$, then analyzed by using the VESTA code[10].

Supporting Fig. and Tables

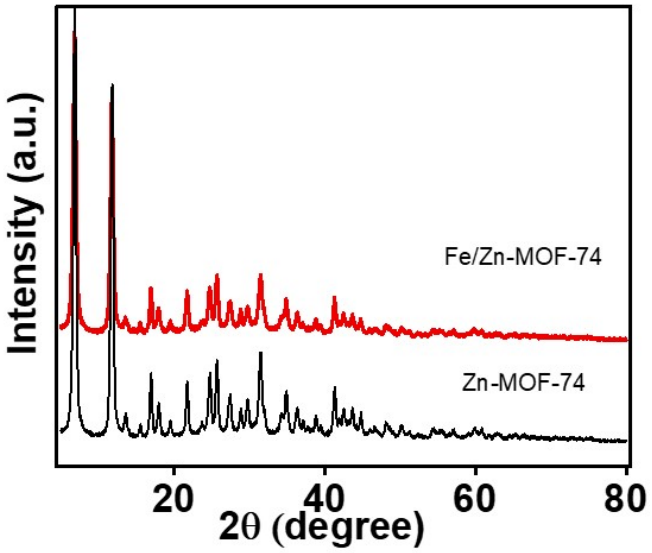

Fig. S1 XRD patterns of Zn-MOF-74 and Fe/Zn-MOF-74.

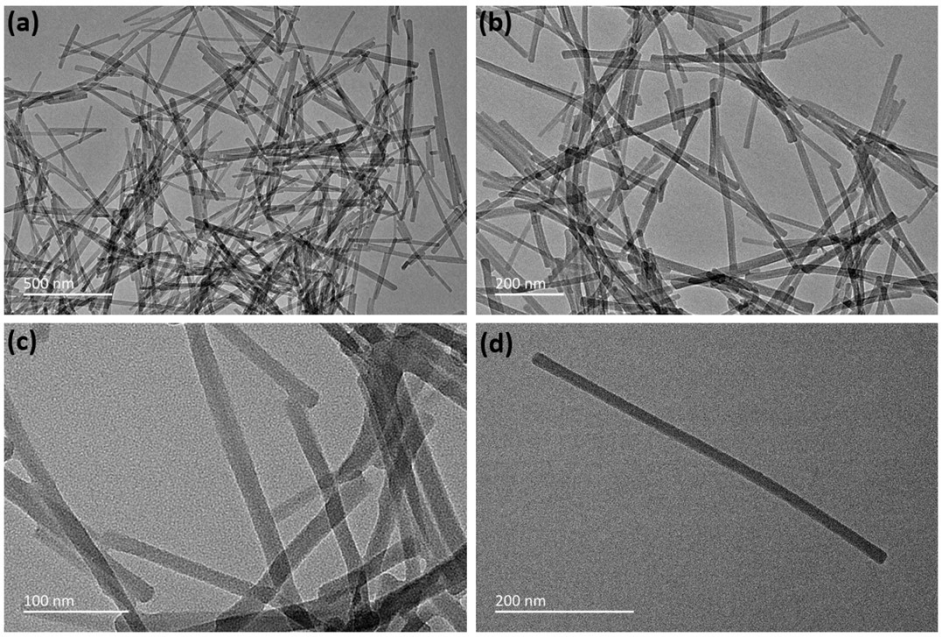

Fig. S2 TEM images of Fe/Zn-MOF-74 with different magnifications.

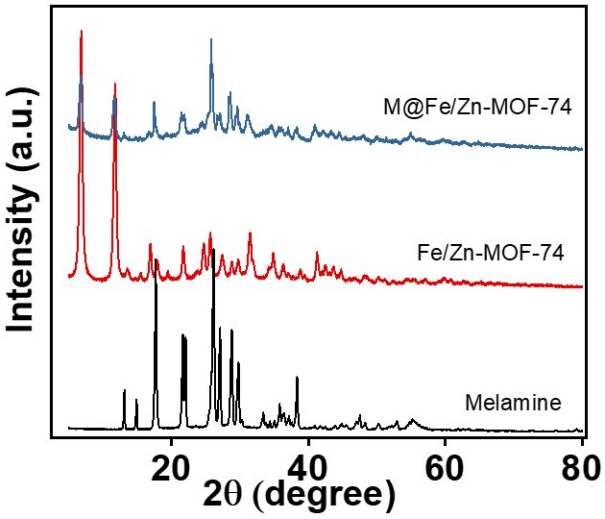

Fig. S3 XRD patterns of Fe/Zn-MOF-74, M@Fe/Zn-MOF-74 melamine and melamine.

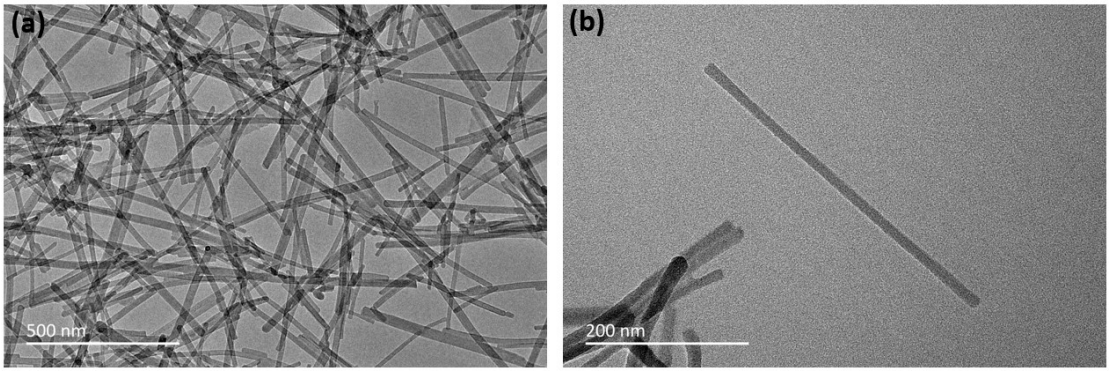

Fig. S4 TEM images of M@Fe/Zn-MOF-74.

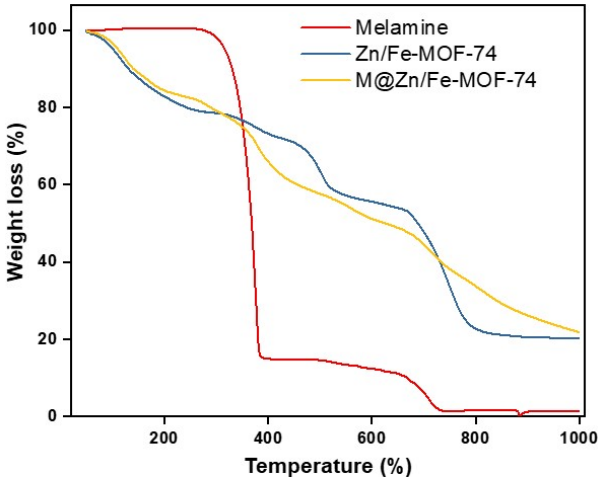

Fig. S5 TGA curves of the melamine, Fe/Zn-MOF-74 and M@Fe/Zn-MOF-74. For melamine, an abrupt mass loss happens at about 380 °C, leading to the weight percent of melamine decreased to only 15%, which was attributed to decomposition of melamine. When the temperature increased to above 730 °C, almost no mass was left. In addition, compared with pure Fe/Zn-MOF-74, in the temperature range of 350 °C

and 725 °C, the M@Fe/Zn-MOF-74 precursor has more mass loss, which is attributed to decomposition of melamine. However, when the temperature continues to increase above 725 °C, the M@Fe/Zn-MOF-74 precursor reserved more mass. This result further reveals that melamine can enhance the stability of the Fe/Zn-MOF-74 structure.

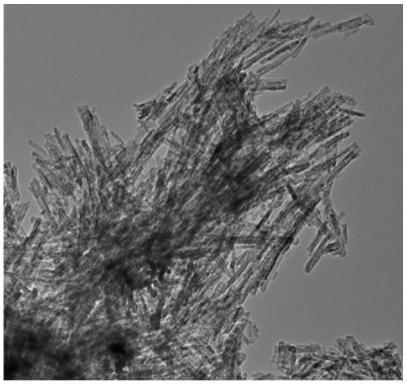

Fig. S6 TEM images of $Fe_1N_2O_2$/NC.

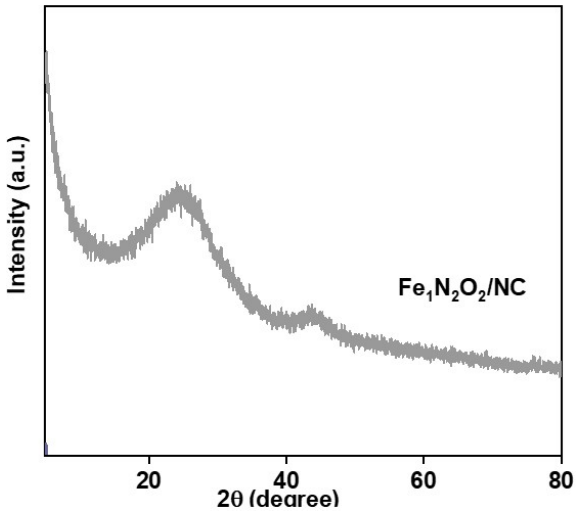

Fig. S7 XRD patterns of $Fe_1N_2O_2$/NC and Fe_n/C.

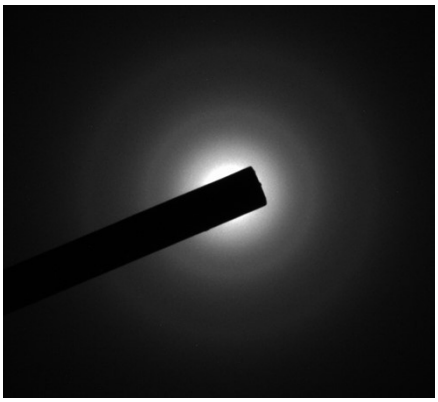

Fig. S8 The ring-like selected area electron diffraction (SAED) image of $Fe_1N_2O_2$/NC catalyst.

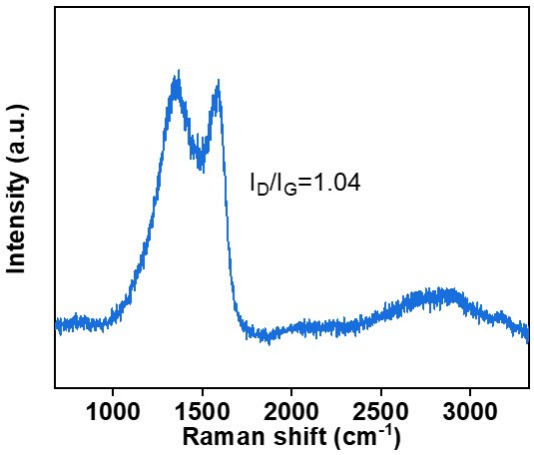

Fig. S9 Raman spectra of $Fe_1N_2O_2$/NC catalyst.

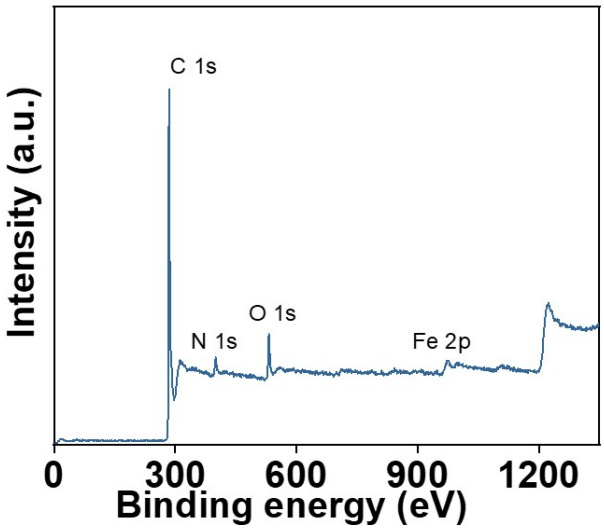

Fig. S10 The XPS survey spectrum of $Fe_1N_2O_2$/NC catalyst.

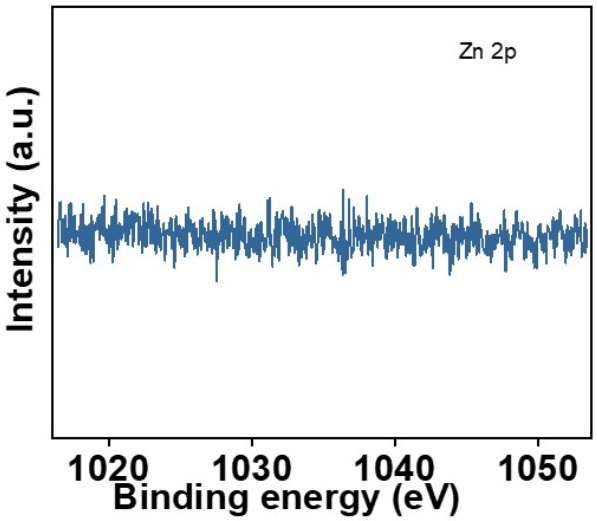

Fig. S11 Zn 2p XPS spectra for $Fe_1N_2O_2$/NC.

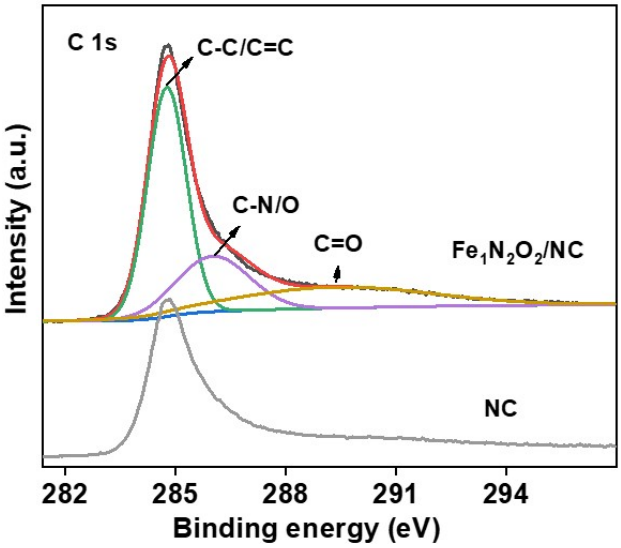

Fig. S12 C 1s XPS spectra for $Fe_1N_2O_2$/NC and NC. The C 1s XPS spectra (Fig. S11) demonstrated three peaks at binding energies of 284.6, 285.4, 286.5, and 288.7 eV, corresponding to graphitic sp^2 carbon (C=C), carbon coordinated with doped O and N (C-N and C-O) , and O=C bonds, respectively.[11] Deconvoluted high-resolution O 1s XPS spectrum (Fig. 2a) displayed the peaks centered at 531.6 eV, 533 eV and 535.7, which could be assigned to the C=O, C-O and adsorbed H_2O, respectively.

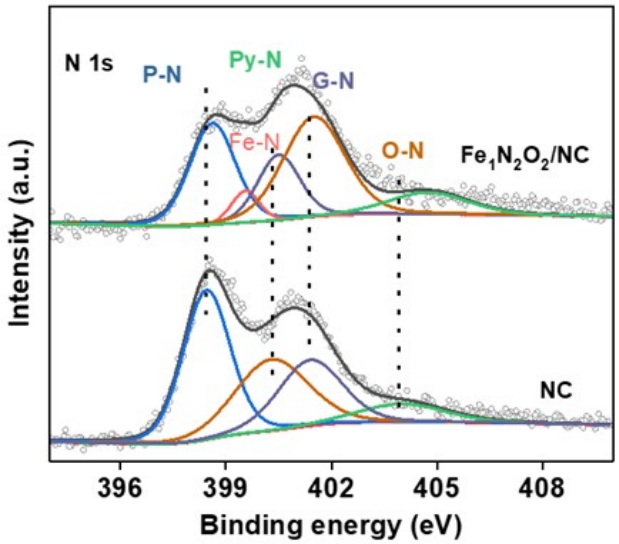

Fig. S13 N 1s XPS spectra for $Fe_1N_2O_2$/NC and N/C. P-N, Py-N, G-N and O-N denote pyridinic N, pyrrolic N, and graphitic N, oxidized-N, respectively. The high-resolution N 1s XPS spectrum of the NC could be divided into five peaks (Fig. S12). Four of them were typical peaks of N-doped carbons located at 398.4, 400.3, 401.5, and 403.8 eV, attributed to pyridinic N (P-N), pyrrolic N (Py-N), graphit (G-N), and oxidized N (O-N), respectively.[12]

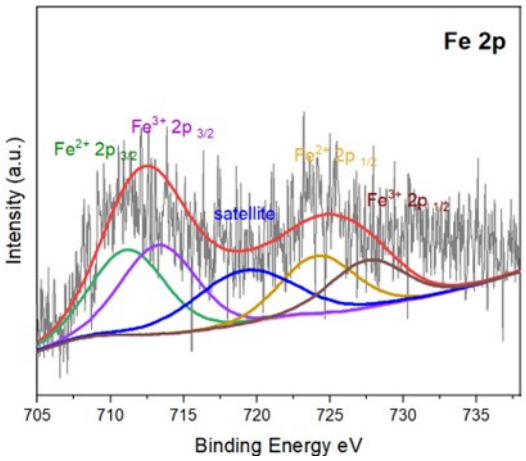

Fig. S14 Fe 2p XPS spectra for $Fe_1N_2O_2$/NC.

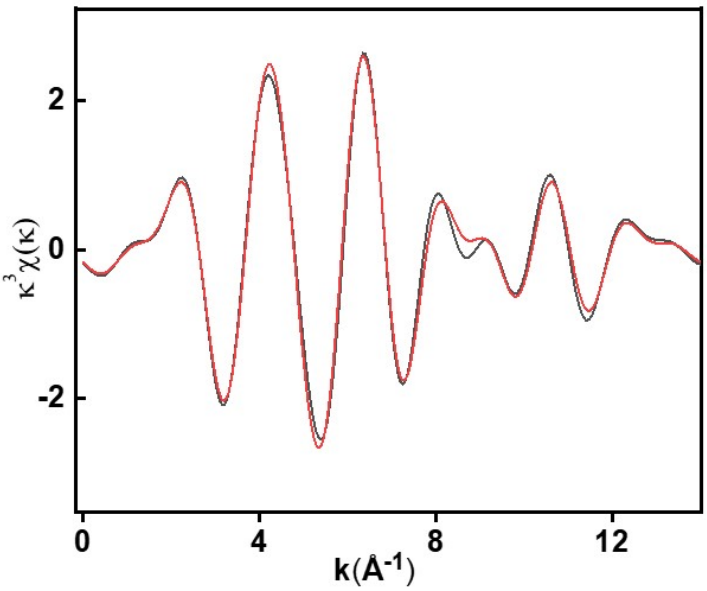

Fig. S15 Fitting of Fourier transformations of EXAFS spectra for $Fe_1N_2O_2$/NC.

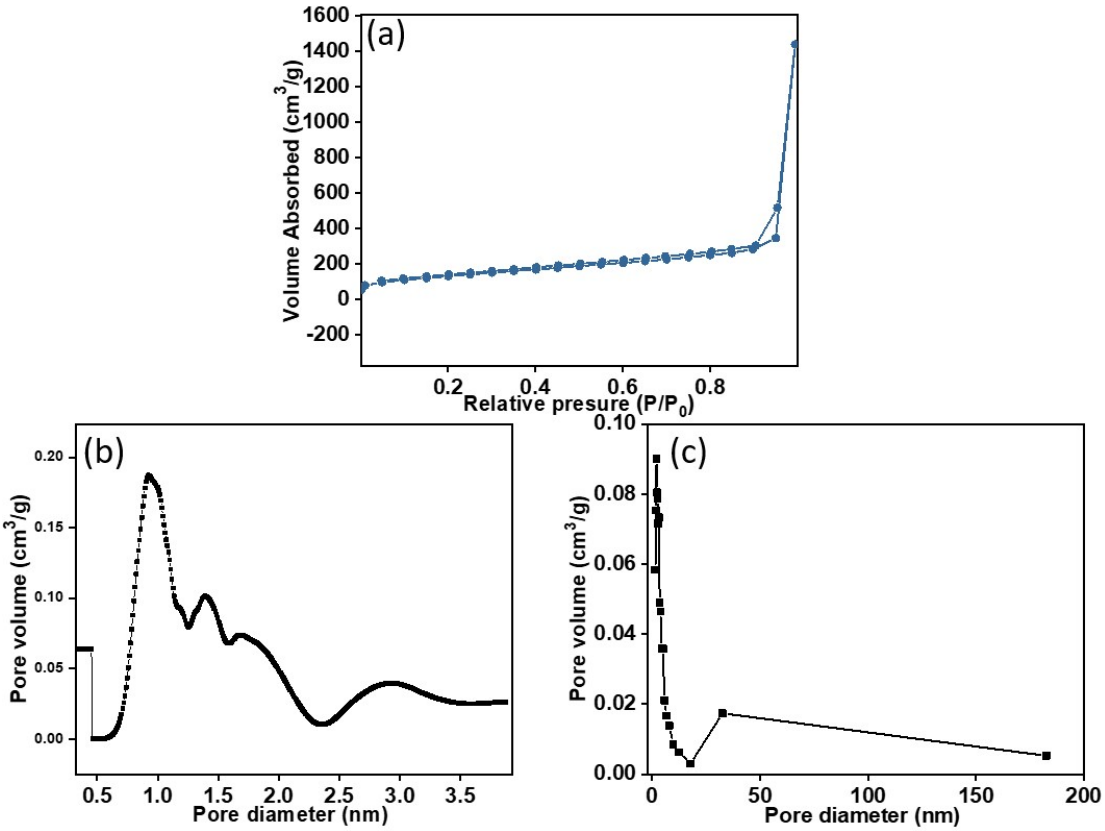

Fig. S16 (a) N_2 adsorption−desorption isotherm of the NC catalyst. The corresponding (b) microporous and (c) mesoporous size distribution curves. As shown in Fig. 3a, the N_2 adsorption−desorption isotherms of Fe/Zn-MOF-74 feature a hysteresis loop (type IV) typical type with a large specific surface area of 1078 m^2 g^{-1} and a pore volume of 2.4 cm^3 g^{-1}.[1,11b] The pore size distribution confirms the coexistence of micro- (~ 0.95 nm) and mesopores (~32.3 nm). After filling melamine, its pores are almost disappeared. Its specific surface area and a pore volume are only 35 m^2 g^{-1} and 0.4 cm^3 g^{-1}, respectively. Interestingly, after pyrolysis treatment at 1,000 °C in an argon flow, except that its morphology is maintained compared with those of Fe/Zn-MOF-74, these pores have a little shrunk, leading to that the micropore and mesopore are mainly concentrated at ~ 0.93 nm and ~ 31.1 nm, respectively. Consequently, the $Fe_1N_2O_2$/NC catalyst shows a large specific surface area of 498 m^2 g^{-1} and a pore volume of 1.9 cm^3 g^{-1}. The porosity of the $Fe_1N_2O_2$/NC catalyst is beneficial for charge and mass transport for electrocatalysis.[17] However, for Fe_n/C catalyst, which was obtained via pyrolysis Fe/Zn-MOF-74 without melamine filling, the pores in parent were destroyed and show a lower specific surface area and very messy size distributions (Fig. S15). Meanwhile, we can see that its morphology was damaged and some FeO_x impurity peak appeared (its SEM, XRD, XANES and EXAFS spectroscopy were shown in Fig. S16-18). These results indicate melamine can not only provide nitrogen source for doping carbon and fixing Fe ions but also help to keep the structure stable.

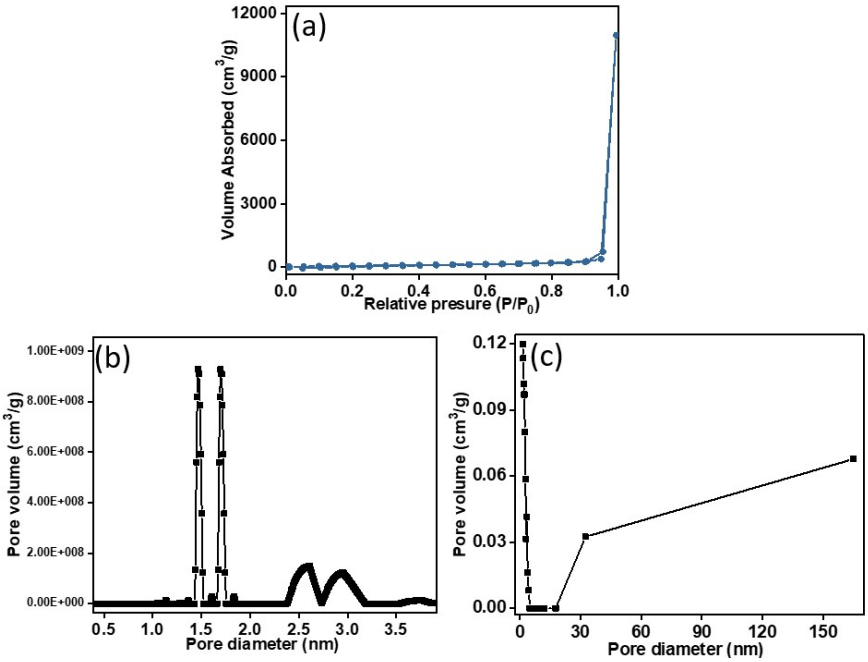

Fig. S17 (a) N_2 adsorption–desorption isotherm of the Fe_n/C catalyst. The corresponding (b) microporous and (c) mesoporous size distribution curves.

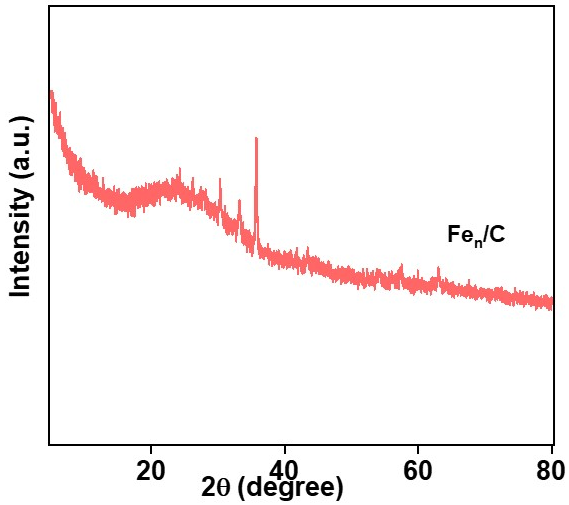

Fig. S18 XRD patterns of Fe_n/C.

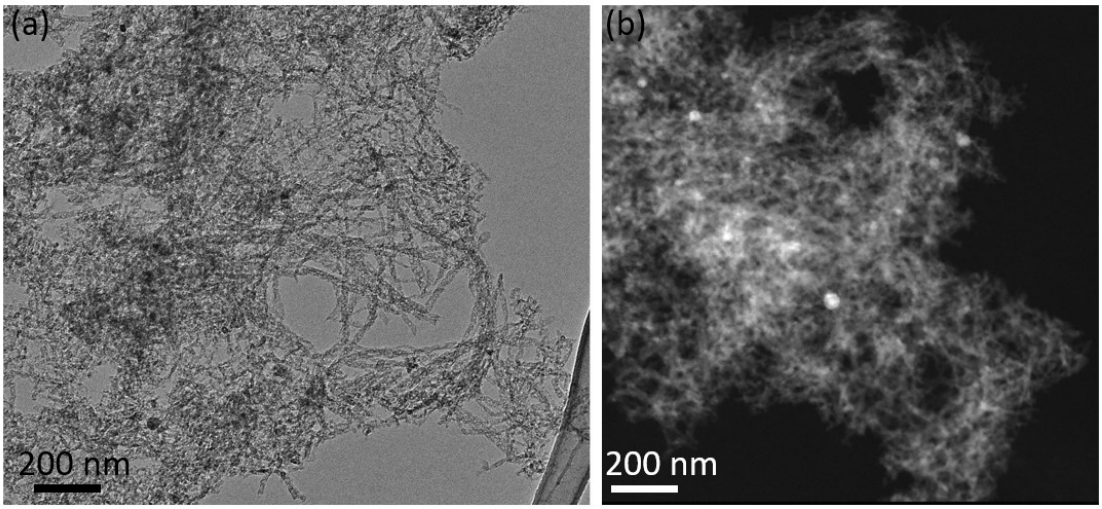

Fig. S19 TEM images of Fe_n/C.

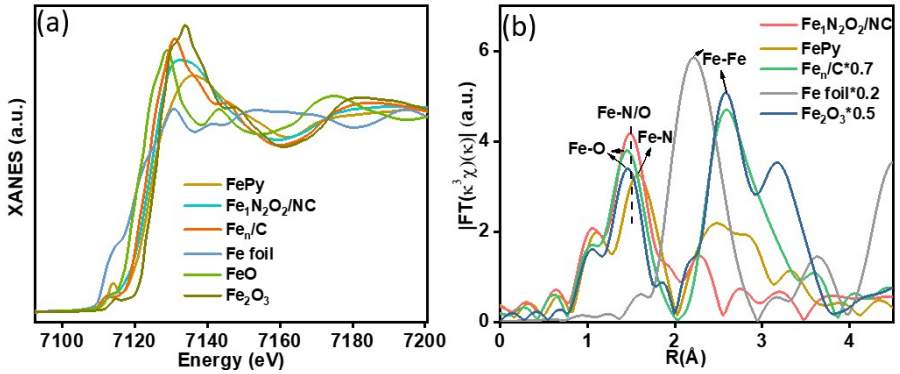

Fig. S20 (a) Fe K-edge XANES spectra. (b) FT-EXAFS of Fe K-edge.

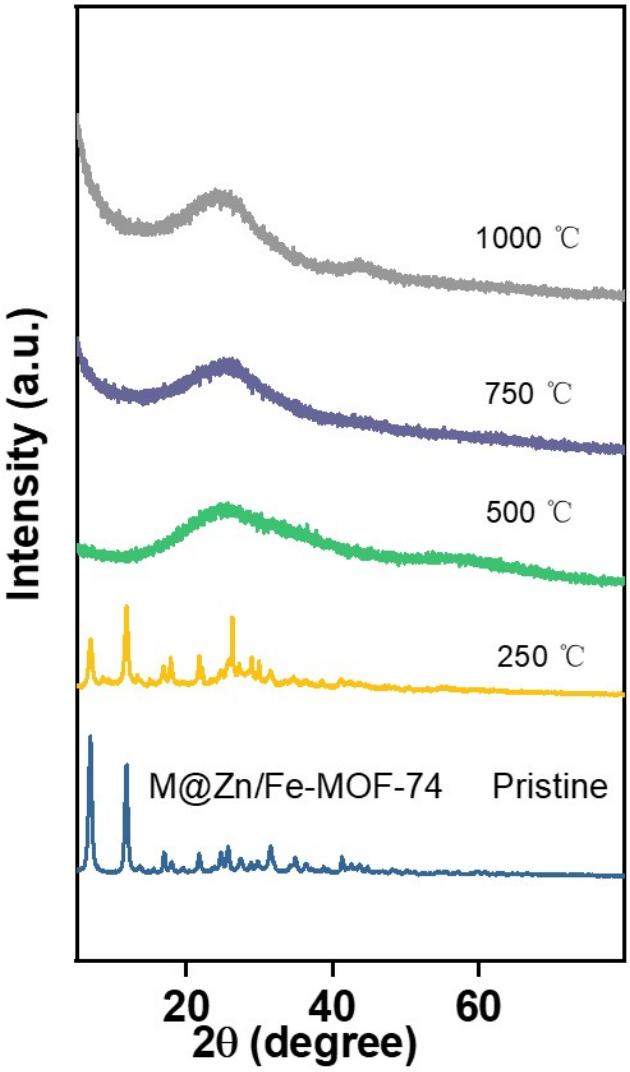

Fig. S21 XRD patterns of the intermediates at different pyrolysis stages of M@Fe/Zn-MOF-74 precursor at 250, 500, 750 and 1000 ℃ in an Ar flow.

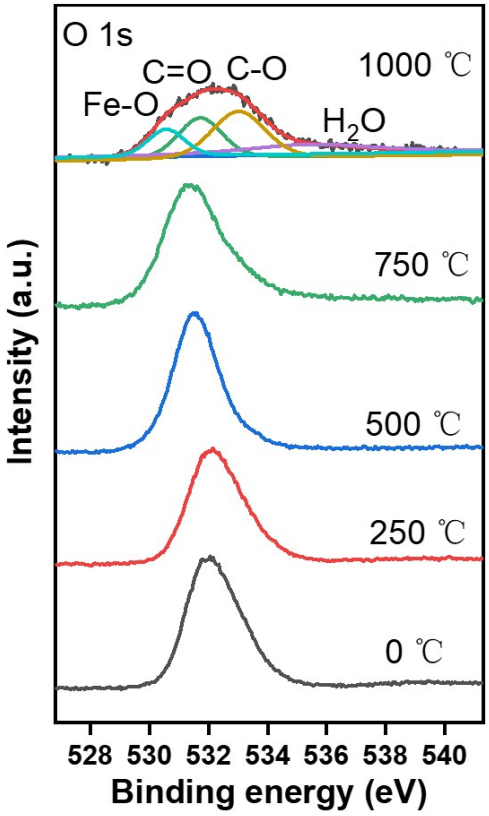

Figure S22 O 1s XPS spectra of the intermediates at different pyrolysis stages of M@Fe/Zn-MOF-74.

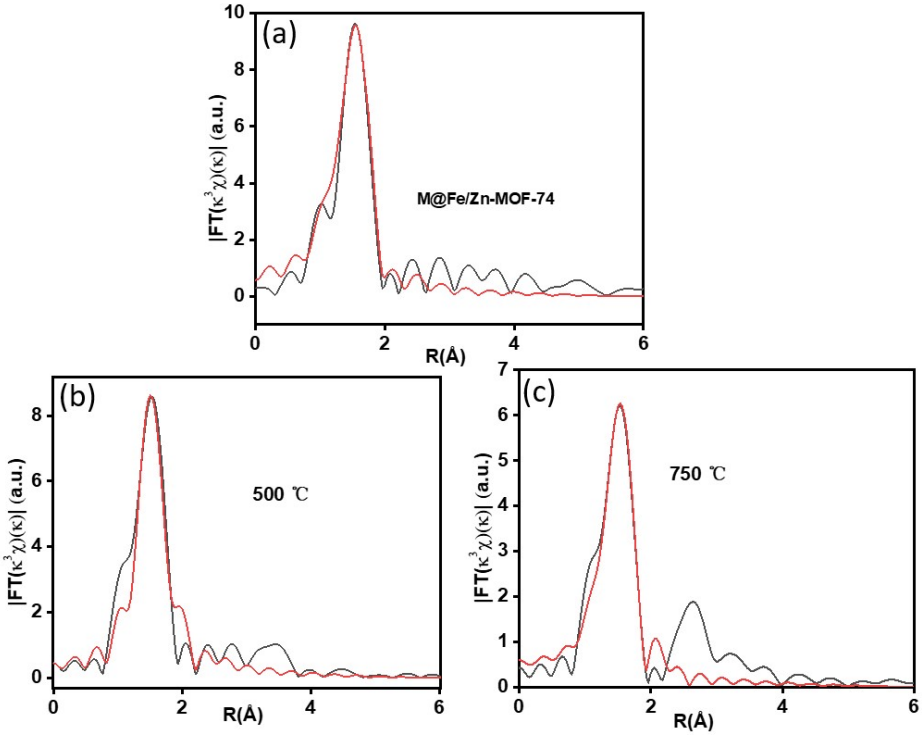

Fig. S23 FT-EXAFS fitting curve for intermediates of M@Fe/Zn-MOF-74 pyrolysis at stages of 0, 500 and 750 ℃.

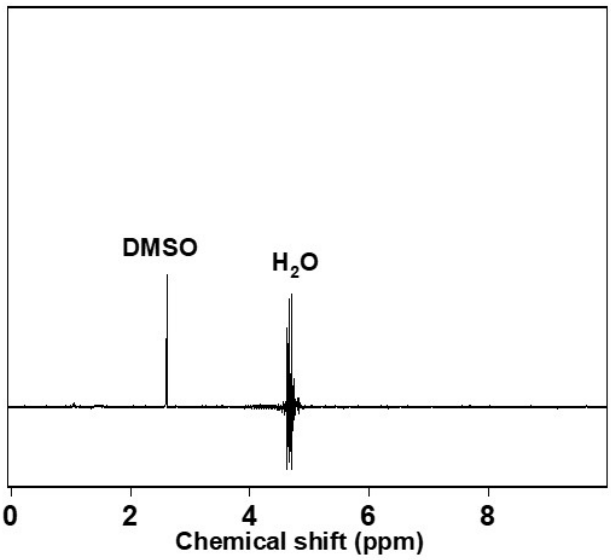

Fig. S24 Characterization for the liquid product of $Fe_1N_2O_2$/NC after 1 h CO_2 reduction process at -0.5 V vs RHE by nuclear magnetic resonance spectroscopy.

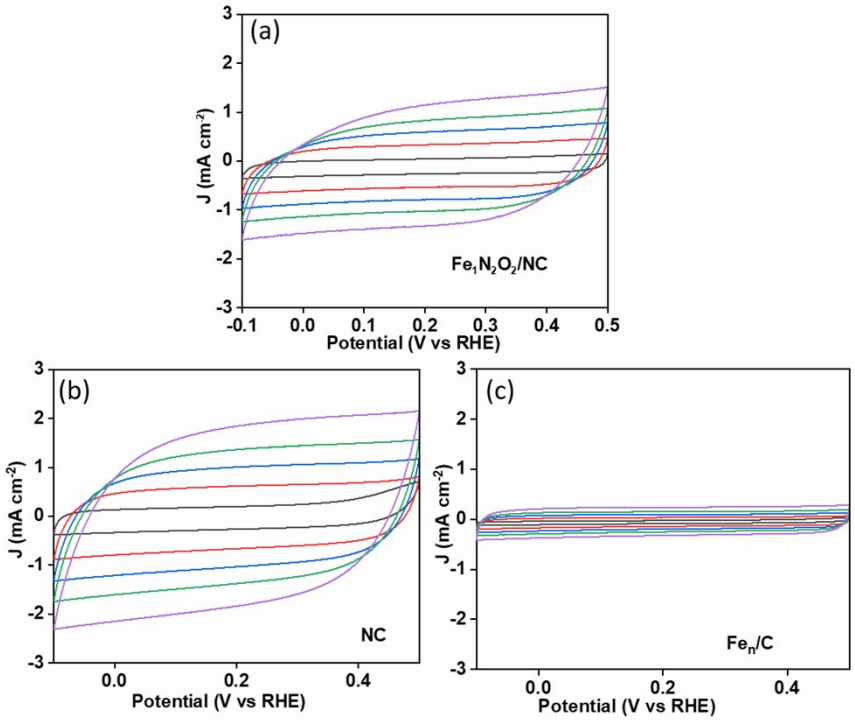

Fig. S25 The electrochemical capacitance measurements of (a) $Fe_1N_2O_2$/NC, (b) NC, and (c) Fe_n/C at various scan rates of 1, 3, 5, 7 and 10 mV s^{-1}.

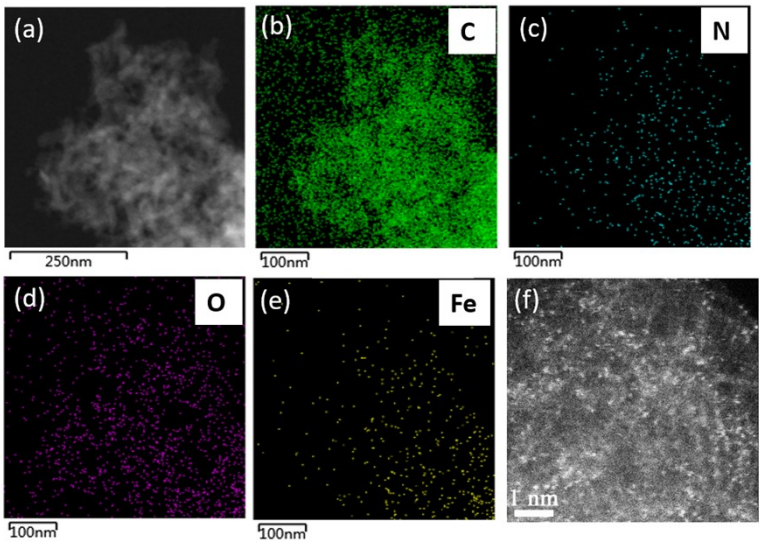

Fig. S26 (a-e) TEM element mapping and (f) HADDF-STEM of the used $Fe_1N_2O_2$/NC catalyst.

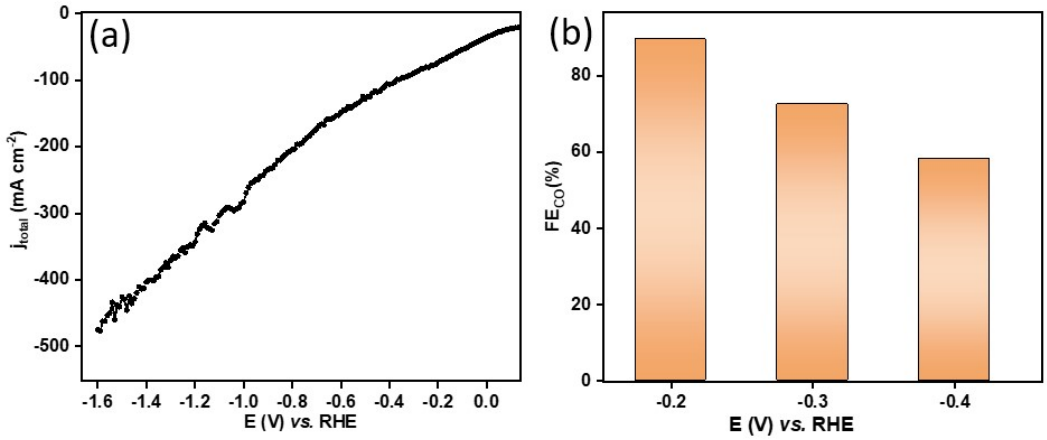

Fig. S27 (a) LSV curves and (b) FE_{CO} at different applied potentials in the flow cell, respectively.

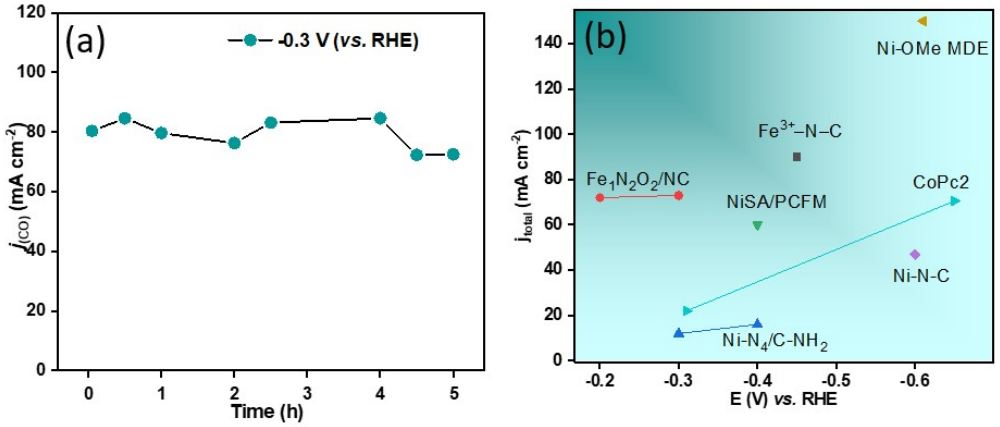

Fig. S28 (a) j_{CO} of long - term stability of $Fe_1N_2O_2$/NC catalyst in 1 M KOH. (b) j_{CO} of $Fe_1N_2O_2$/NC in comparison with other reported carbon-based non-noble metal single-atomic site CO_2RR electrocatalysts in the flow cell.

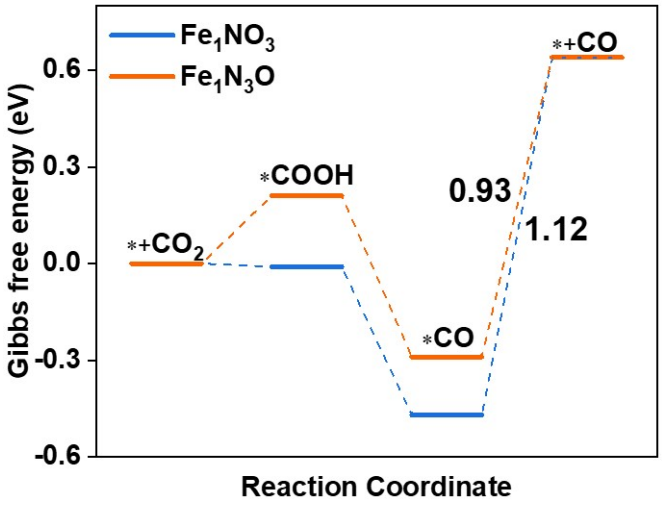

Fig. S29 Gibbs free energy change of CO_2RR pathways on Fe sites of Fe_1NO_3 and Fe_1N_3O.

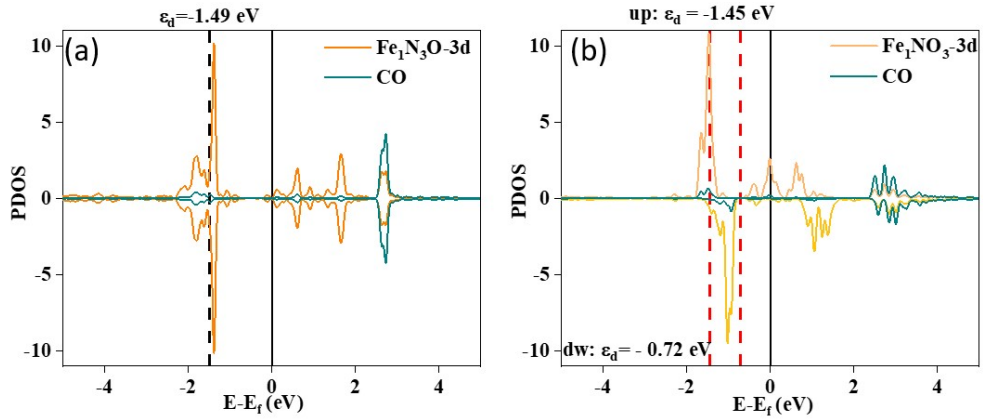

Fig. S30 PDOS graphs of 3d orbitals of Fe atoms on (a) CO@Fe_1N_3O, and (b) CO@Fe_1NO_3. The black or red dash lines show the average d-band center (ε_d). The spin-polarization was considered and the Fermi level was taken as zero of energy. The up and dw express the spin up and spin down of Fe_1NO_3.

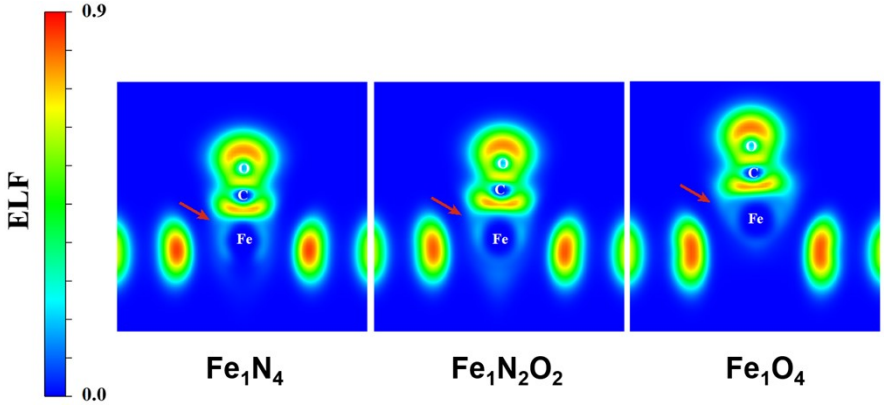

Fig. S31 Electron localization function (ELF) of CO@Fe_1N_4, CO@$Fe_1N_2O_2$ and CO@Fe_1O_4. The red small arrows showed that the difference of relatively covalent binding interaction between CO@Fe_1N_4 and CO@$Fe_1N_2O_2$ and CO@Fe_1O_4.

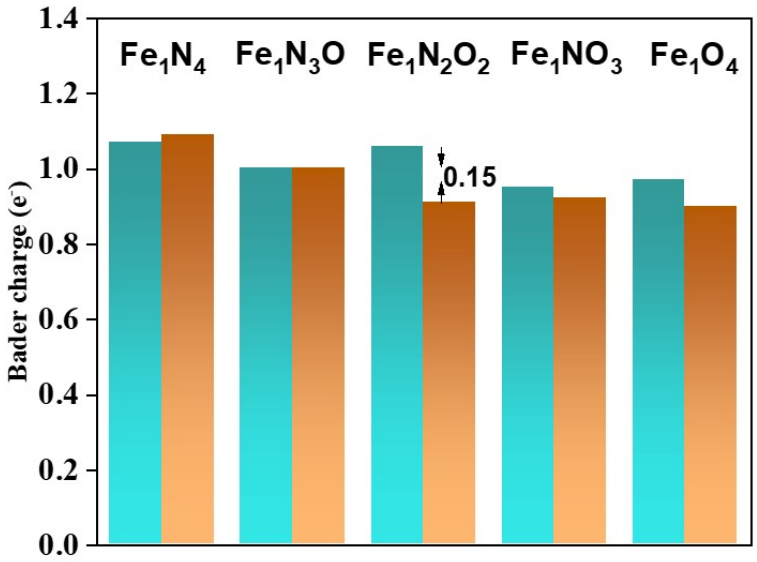

Fig. S32 The number of Bader charges transfer at Fe sites in CO@Fe_1N_4 and Fe_1N_4 slab, CO@Fe_1N_3O and Fe_1N_3O slab, CO@$Fe_1N_2O_2$ and $Fe_1N_2O_2$ slab, CO@Fe_1NO_3 and Fe_1NO_3 slab, CO@Fe_1O_4 and Fe_1O_4 slab, respectively. The negative value of Bader charges represents Fe sites lose electrons, and the * refers to the catalytic slab, and the *one refers to the species that adsorbed on the activity sites.

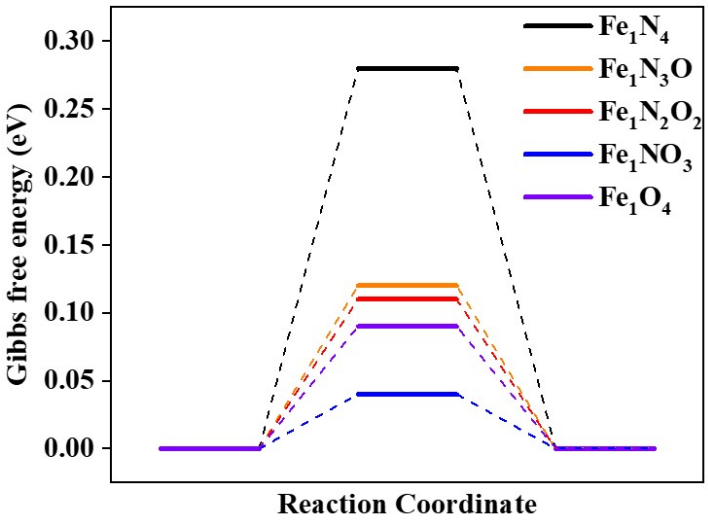

Fig. S33 HER pathways on Fe sites of different catalyst configuration.

Table S1 | Structural parameters of $Fe_1N_2O_2$/NC extracted from the EXAFS fitting. (S_0^2=0.85)

Sample	Scattering pair	CN	R(Å)	$\sigma^2(10^{-3}Å^2)$	ΔE_0(eV)	R
M@Fe/Zn-MOF-74	Fe-O	6.0(3)	1.94(2)	5.0(5)	-5.4(2)	0.02
500	Fe-O	5.2(5)	1.94(2)	5.2(5)	-5.4(2)	0.02
750	Fe-O	2.9(4)	1.93(2)	5.6(4)	-5.4(2)	0.02
	Fe-N	1.8(2)	1.91(2)	6.2(3)	-5.4(2)	0.02
$Fe_1N_2O_2$/NC	Fe-O	2.1(4)	1.92(2)	5.8(4)	-5.4(2)	0.02
	Fe-N	2.0(1)	1.91(2)	5.9(4)	-5.4(2)	0.02

S_0^2 is the amplitude reduction factor; CN is the coordination number; R is interatomic distance (the bond length between central atoms and surrounding coordination atoms); σ^2 is Debye-Waller factor (a measure of thermal and static disorder in absorber-scatterer distances); ΔE_0 is edge-energy shift (the difference between the zero kinetic energy value of the sample and that of the theoretical model). R factor is used to value the goodness of the fitting.

Table S2 Comparison of CO_2RR performance of $Fe_1N_2O_2$/NC with other representative atomically dispersed Fe active sites embedded in carbon matrix electrocatalysts in the H-type cell.

Sample	**CE[a]**	**E_{CO}>90% /the lowest potential vs RHE (V)**	**Maximum CO FE%/the Potential vs RHE (V)**	**The Potential vs RHE (V) (FE_{CO} > 95%)**	**Current (mA cm^{-2})**	**Ref.**
$Fe_1N_2O_2$ /NC	**Fe-N_2O_2**	**96 / -0.4**	**99.7 / -0.5**	**-0.4 to -0.8**	**-1.3 to -11_{total} -0.5 to -8.6_{co}**	**This work**
Fe^{3+}–N–C	**Fe–X_4 (X = N or C)**	~90 / -0.4	~96 / -0.48	-0.48	**~20_{co}**	Science. 2019, 364, 1091-1094.
H_2–FeN_4/C	**Fe–N_4**	~90 / -0.3	~97 / -0.6	-0.6	**6.87$_{total}$**	Chem. 2021, 7, 1-11.
Fe-SAC/NP	**Fe–N_4**	~90 / ~0.38	97 / -0.53	-0.38 to 0.65	**2.5 to 19$_{co}$**	Angew. Chem. Int.

C						Ed. 2021, 60, 23614-23618.
FeN_4-O_1	**Fe-N_4O_1**	99 / -0.56	99 / -0.56	-0.56 to -0.87	**-5 to -13_{total}**	Energy Environ. Sci. 2021, 14, 3430-3437.
FeN_4/C	**Fe–N_4**	93 / -0.6	93 / -0.6	-0.5 to -0.6	**-1 to -2_{total} -0.6 to -1.2_{co}**	Adv. Sci. 2020, 7, 2001545.
Fe-N3	**Fe–N_3**	~96 / -0.5	96 / -0.5	-0.4 to -0.6	**-3 to -7_{co}**	Adv. Mater. 2020, 32, e2002430.
Fe–N_4	**Fe–N_4**	~90 / -0.5	94 / -0.58	-0.5 to -0.58	**-2 to -5_{co}**	ACS Catal. 2020, 10, 10803-10811.
FeN_5	**Fe–N_5**	97 / -0.46	97 / -0.46	-0.46	**~7_{total}**	Angew. Chem. Int. Ed. 2019, 58, 14871-14876.

[a]CE = Coordination environment.

Table S3. J_{CO} of $Fe_1N_2O_2$/NC in comparison with those of other reported carbon-based non-noble metal single-atomic site CO_2RR electrocatalysts in the flow cell.

Sample	Electrolyte	Potential (V vs. RHE) [a]	J_{CO} (mA cm^{-2})	FE_{CO} (%)	Ref.
A-Fe@NG-Li_1K_3	1.0 M KOH	-0.2	73	91	This work
Fe^{3+}-N-C	0.5 M $KHCO_3$	-0.45	94	90	Science. 2019, 364, 1091-1094.
Ni-N_4/C-NH_2	1.0 M KOH	-0.3	~12	65	Energy Environ. Sci., 2021, 14, 2349-2356.
		-0.4	~16	78	
NiSA/PCFM	0.5 M $KHCO_3$	-0.4	60	54	Nat. Commun. 2020, 11, 593.
Ni-N-C	1.0 M $KHCO_3$	-0.6	~47	-	Energy Environ. Sci., 2019, 12, 640-647.
Ni-OMe MDE	1.0 M $KHCO_3$	-0.61	150	99.8	Nat. Energy, 2020, 5, 684-692.
		-0.31	22	93	Nat. Commun. 2019,

	-0.65	70.5	94	

(Note: [b] is the CO partial current density under the potential [a].)

REFERENCES

[1] P. Pachfule, D. Shinde, M. Majumder, Q. Xu, *Nat. Chem.* **2016**, *8*, 718-724.

[2] a) G. Kresse, J. Furthmu¨ller, *Phys. Rev. B* **1996**, *54*, 11169; b) G. Kresse av, J. Furthmiiller, *Comput. Mater. Sci.* **1996**, *6*, 15-50.

[3] G. Kresse, D. Joubert, *Phys. Rev. B* **1999**, *59*, 1758.

[4] John P. Perdew, Kieron Burke, M. Ernzerhof, *Phys. Rev. Lett.* **1996**, *77*, 3865-3868.

[5] S. Grimme, J. Antony, S. Ehrlich, H. Krieg, *J. Chem. Phys.* **2010**, *132*, 154104.

[6] W. Setyawan, S. Curtarolo, *Comput. Mater. Sci.* **2010**, *49*, 299-312.

[7] V. Wang, N. Xu, J.-C. Liu, G. Tang, W.-T. Geng, *Comput. Phys. Commun.* **2021**, *267*.

[8] My Hang V. Huynh, Thomas J. Meyer, *Chem. Rev.* **2007**, *107*, 5004−5064.

[9] a) J. K. Norskov, F. Abild-Pedersen, F. Studt, T. Bligaard, *PNAS* **2011**, *108*, 937-943; b) S. J. Hwang, S. K. Kim, J. G. Lee, S. C. Lee, J. H. Jang, P. Kim, T. H. Lim, Y. E. Sung, S. J. Yoo, *J. Am. Chem. Soc.* **2012**, *134*, 19508-19511.

[10] K. Momma, F. Izumi, *J. Appl. Crystallogr.* **2008**, *41*, 653-658.

[11] a) N. Xiao, S. G. Liu, S. Mo, N. Li, Y. J. Ju, Y. Ling, N. B. Li, H. Q. Luo, *Talanta* **2018**, *184*, 184-192; b) K. Yuan, D. Lutzenkirchen-Hecht, L. Li, L. Shuai, Y. Li, R. Cao, M. Qiu, X. Zhuang, M. K. H. Leung, Y. Chen, U. Scherf, *J. Am. Chem. Soc.* **2020**, *142*, 2404-2412.

[12] a) H. B. Yang, S. F. Hung, S. Liu, K. Yuan, S. Miao, L. Zhang, X. Huang, H. Y. Wang, W. Cai, R. Chen, J. Gao, X. Yang, W. Chen, Y. Huang, H. M. Chen, C. M. Li, T. Zhang, B. Liu, *Nat. Energy* **2018**, *3*, 140-147; b) X. Wang, Y. Wang, X. Sang, W. Zheng, S. Zhang, L. Shuai, B. Yang, Z. Li, J. Chen, L. Lei, N. M. Adli, M. K. H. Leung, M. Qiu, G. Wu, Y. Hou, *Angew. Chem. Int. Ed.* **2020**, *60*, 4192-4198.

[13] D. Hursán, A. A. Samu, L. Janovák, K. Artyushkova, T. Asset, P. Atanassov, C. Janáky, *Joule* **2019**, *3*, 1719-1733.